Experimental Mechanics
https://doi.org/10.1007/s11340-026-01336-9

RESEARCH PAPER

Strain Mapping in the Vicinity of Cracks Using a Conical Slit Setup for Angular Dispersive Synchrotron X-Ray Diffraction

F. Loebich[1] · N. Möller[2] · J. Richter[2] · T. Wegener[3] · D. Canelo-Yubero[4] · E. Maawad[4] · N. Schell[4] · J. Gibmeier[1] · T. Niendorf[2]

Received: 22 December 2025 / Accepted: 5 June 2026
© The Author(s) 2026

Abstract

Background Laser-based powder bed fusion (PBF-LB/M) is a manufacturing technique that enables tailoring of the properties of components towards the application, provided the process parameters are adjusted. However, the process induces residual strain and stresses, influencing, i.e., the fatigue properties. To analyze the residual strain distributions in the vicinity of fatigue cracks in the bulk of specimens a high lateral resolution is necessary, which limits the possible analysis methods to high-energy synchrotron X-ray diffraction.

Objective The objective is to propose a viable strategy to determine the (lattice) strain distributions in the vicinity of fatigue cracks in AISI 316L compact-tension specimens manufactured via PBF-LB/M.

Methods An angular dispersive high-energy synchrotron X-ray diffraction setup with conical slits is used, to restrict the gauge volume to the center of the specimens. Complementarily, the residual stress distribution near the surface is investigated using the incremental hole-drilling method.

Results Along the build direction a compressive residual strain distribution of higher magnitude is found, which is significantly reduced in the vicinity of the crack. Depending on whether the crack opening direction is aligned with the transverse or the build direction, a tensile lattice strain field or a lattice strain field of reduced magnitude is found ahead of the crack tip.

Conclusions The results indicate that the proposed strategy is well suited to determine the (lattice) strain distributions in the vicinity of fatigue cracks in the center of the specimens with a sufficient lateral resolution.

Keywords PBF-LB/M · Fatigue cracks · Synchrotron X-ray diffraction · Conical slit · Residual stress

Introduction

Laser-based powder bed fusion (PBF-LB/M) is an additive manufacturing process used to build metal components from 3D computer-aided design files. To achieve this, metal powder is molten layer by layer locally along the component geometry. In case of PBF-LB/M, a laser beam is used for the local heat input to melt the metal powder [1–3]. The variation of process parameters such as laser power, scan speed, laser beam profile or hatch distance enables tailoring of the microstructure and therefore the mechanical properties of the components towards the desired application [4].

Since the process parameters can be varied while building the component, the component's microstructure can also be adjusted, enabling for instance a defined microstructural grading to tailor the component's performance with respect to the application needs. This was shown in [5] for IN718 and in [6] for the stainless steel AISI 316L where a dual

✉ F. Loebich
florian.loebich@kit.edu

1 Institute for Applied Materials (IAM-WK), Karlsruhe Institute of Technology (KIT), Engelbert-Arnold-Straße 4, 76131 Karlsruhe, Germany

2 Institute of Materials Engineering – Metallic Materials, University of Kassel, Mönchebergstraße 3, 34125 Kassel, Germany

3 Center for Structural Materials (MPA-IfW), Technical University of Darmstadt, Otilie-Bock-Straße 3, 64287 Darmstadt, Germany

4 Helmholtz-Zentrum Hereon, Max-Planck-Str. 1, 21502 Geesthacht, Germany

Published online: 18 June 2026

laser system with different nominal laser powers of 400 W and 1 kW as well as different beam shapes (i.e., a Gaussian profile and a top-hat profile for the 400 W and 1 kW laser, respectively) and specifically adjusted process parameters were used to achieve two distinctive microstructural regions within a single component: one fine-grained, equiaxed and less textured microstructure by the 400 W laser and one coarse-grained, columnar and strongly textured microstructure by the 1 kW laser. This enables not only the change in mechanical properties within different microstructural regions but also affecting the fatigue properties of the whole component. Brenne and Niendorf [7] investigated the crack growth behavior in compact tension (CT) specimens with a microstructural gradient obtained by the dual laser system. The authors were able to show that the crack growth rate in a specimen, where the crack grows perpendicular to the longer grain axis, can significantly be decreased when entering the region of the coarse-grained microstructure produced by the 1 kW laser. This was attributed to the higher crack deflection in the coarse-grained microstructure compared to the fine-grained microstructure. However, in this early work the influence of the residual stress (RS) distribution within the microstructurally graded component induced during processing remained unconsidered.

The fundamental process principle of PBF-LB/M, i.e., local melting of the powder followed by subsequent cooling, causes a high thermal gradient and rapid cooling near the melt pool. As a result, in components built using PBF-LB/M significant RS are present due to those gradients and the thermal cycles leading to localized compression and tension [8, 9]. The resulting RS within a component are, analogous to the microstructure, significantly influenced by the process parameters. For example, an increase in laser power, and thereby energy input, can lead to higher levels of RS, due to the larger melt pool dimensions resulting in a steeper temperature gradient [10]. A faster scan speed reduces the interaction time leading to a smaller melt pool and higher cooling rates resulting in higher RS levels [11]. As another factor, the hatch distance determining the amount of overlapping between adjacent scan paths has a significant effect on the thermal history as the temperature accumulation is reduced, when the hatch distance is increased. [12, 13]. The resulting RS also depend on the scanning strategy, since the RS are highest along the scan path [14, 15]. Therefore, it is beneficial to change the scan direction every layer, reducing the RS compared to unidirectional scanning [16, 17].

RS play a significant role in the behavior of materials under fatigue loading, especially in the context of fatigue crack growth [18]. Tensile RS near the crack tip usually accelerate crack growth, as they superimpose with the applied external stress [19, 20]. In contrast, compressive RS can be beneficial by decreasing the crack growth rate [21, 22]. However, the RS distribution is not necessarily stable during fatigue loading, instead it may be subject to changes during crack propagation [23, 24]. To evaluate the role of RS on the crack growth behavior, it is therefore necessary to determine the RS state in the vicinity of cracks, especially when dealing with complex RS distributions as developed during PBF-LB/M processing of components.

When analyzing the stress or strain distribution in the vicinity of cracks, a high spatial resolution is necessary due to the size of the areas of interest and the locally prevailing features, respectively. In addition, usually information from the inner bulk of the specimens is of higher interest rather than information from the near surface area. Laboratory X-ray diffraction techniques are usually limited to the very near surface area, since the achievable penetration depth is comparatively low [25]. This leaves neutron diffraction [23, 26, 27] and high-energy synchrotron X-ray diffraction [28–31] as possible methods. For high-energy synchrotron X-ray diffraction setups in general, angular as well as energy dispersive approaches, mostly applied in transmission mode, can be used to gain diffraction data from the bulk of the components. Energy-dispersive X-ray diffraction (EDXRD) using high-energy synchrotron radiation is an important tool for analyzing RS in a localized area within a component, since the setup already masks a small measurement volume through the slit apertures used in the primary and secondary beam paths. Moreover, by using a two or even more detector setup, lattice strains can be analyzed in two or more directions simultaneously [25].

In direct comparison, monochromatic high-energy synchrotron X-ray diffraction, i.e., using an angular dispersive setup, enables the detection of complete Debye–Scherrer rings, which is especially beneficial when investigating textured or coarse-grained materials. A drawback of conventional monochromatic synchrotron X-ray diffraction transmission setups with respect to the analysis of strain distributions in the vicinity of cracks is the fact that the diffraction information stems from the entire specimen thickness. As the gauge volume cannot be adjusted along the beam direction, an integrated diffraction information along the beam path through the component is recorded. As a result, near surface gradients in the stress or strain distribution contribute to the diffraction result. A solution to overcome this drawback, and to define a limited gauge volume along the beam path using monochromatic high-energy synchrotron X-ray diffraction, is offered by using either a conical slit [32–34], a spiral slit [35] or a 'spider-web slit' [36]. Conical slits, which are most often applied for this purpose, have a conical opening with a constant gap size and are positioned between the specimen and the detector. The depth resolution, i.e. the resolution in beam direction, depends on the design of the conical slit, particularly it's gap size, as well as on the distance between specimen and conical slit, the beam size and the beam

energy, respectively. While the gap size of the conical slit is typically fixed by design, the other parameters can be adjusted according to the requirements, although the beam energy and the distance between specimen and conical slit cannot be chosen independently as they are mutually dependent. Since one conical slit only allows one specific Debye–Scherrer cone to pass, multiple conical slits (slit cell) are required to analyze the Debye–Scherrer rings of multiple {hkl}-crystallographic planes.

To evaluate the so far unconsidered effect of RS on reduced fatigue crack growth rates due to a microstructure gradient as reported in [7], it is necessary to determine the RS distribution in the vicinity of the crack and how it changes during crack growth. The RS distribution in the center of the specimens is of particular interest in this regard, which cannot be easily determined using laboratory methods. The determination of the RS distribution in the vicinity of cracks additionally requires a high lateral resolution, which can only be achieved by high-energy synchrotron X-ray diffraction. For neutron stress analysis, the spatial resolution is not sufficient. A preliminary study of the authors' group investigating microstructural properties as well as the RS distribution in the as-built state [37] has already revealed additional challenges with respect to the determination of the RS distribution.

The local microstructure, which in some areas is characterized by large grains and crystallographic texture induced by the PBF-LB/M process, must be taken into account in diffraction experiments. This further limits the use of neutron diffraction and EDXRD since full Debye–Scherrer rings cannot be recorded without additional effort. Instead, angular dispersive high-energy synchrotron X-ray diffraction in combination with a 2D-detector allows for the detection of full Debye–Scherrer rings. Furthermore, the preliminary investigation revealed a significant in-depth gradient in the RS distribution from the surface to the center of the specimen. This requires a restriction of the gauge volume to the center, which can be achieved using conical slits as previously explained.

In the present work, the strain distributions in the vicinity of fatigue cracks in PBF-LB/M manufactured AISI 316L specimens were investigated. In order to assess the general suitability of the proposed measuring and evaluation strategy, CT-specimens from the region showing a smaller grain size and a less pronounced crystallographic texture without a distinct microstructure gradient as described in [7, 37] are assessed here. The RS distribution near the surface in a condition being derived from classical CT-specimens was analyzed using the incremental hole-drilling (IHD) method, as it is a reliable and standardized RS analysis method [38, 39]. That enables a higher information depth than other laboratory methods, while also being able to consider the effect of crystallographic texture, when an adapted evaluation strategy using a case sensitive calibration is applied [40]. The (residual) strain distribution maps in the vicinity of the crack in the center of the specimens were determined using a conical slit setup for high-energy synchrotron X-ray diffraction in transmission mode. This approach allowed to assess the viability of the chosen setup and evaluating strategy to overcome the above-mentioned challenges. To correlate cracks and the determined strain distributions, the crack paths were determined using X-ray computed tomography scans.

Material and Methods

Material and Specimen Geometry

The investigated specimens were built from AISI 316L stainless steel via PBF-LB/M. Rectangular tube profiles, as depicted in Fig. 1(a) with a wall thickness of 4 mm and the dimensions of 40 mm in length, width and height were built using a SLM280^{HL} machine from SLM Solutions Group AG (Lübeck, Germany). The process parameters for the laser

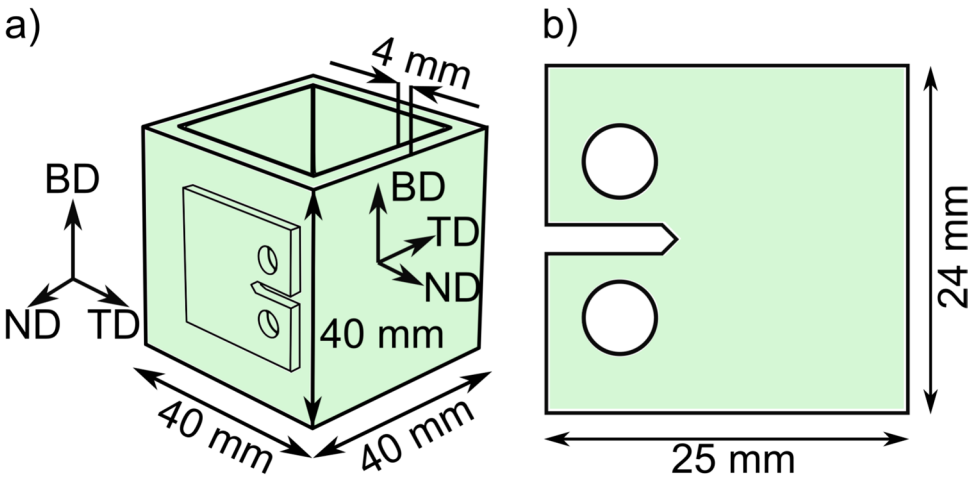

Fig. 1 Specimen geometry: (**a**) rectangular tube profile built using PBF-LB/M, (**b**) compact tension (CT) specimen

with a nominal power of 400 W are reported in a previous study by the authors' group [37].

To characterize the strain distribution in the vicinity of fatigue cracks, CT-specimens, see Fig. 1(b), with the dimensions 25 mm × 24 mm × 4 mm were cut out of the wall of these rectangular tube profiles by wire-EDM (electrical discharge machining). All specimens investigated were in the as-built state, i.e., no post treatment on the surface was conducted. The CT-specimens were cyclically loaded using a constant load range of 800 N at a load ratio of R = 0.1. The crack growth was monitored using the potential drop method and after reaching a crack length of around 6 mm measured from the notch tip, the loading sequence was stopped. The crack growth direction was either parallel to the build direction (BD) or perpendicular (transversal direction, TD). Figure 1(a) illustrates exemplary the orientation of a CT-specimen where the crack growth direction is along TD. For crack growth along BD the CT-specimen is rotated accordingly. BD, TD (and ND) form a side-specific coordinate system not a global coordinate system, with ND being the respective side surface normal.

The microstructure is shown in Fig. 2(a) by a SEM-BSE image (SEM = scanning electron microscope, BSE = back scattered electrons). Features seen are due to the orientation contrast after etching with V2A-etchant. The micrograph reveals characteristics related to the melt pool boundaries as well as the epitaxial grain growth along the build direction and thus, the most pronounced temperature gradient. A more detailed investigation of the microstructure can be found in [37], where the grain morphology was determined to be direction dependent with sizes around 73 × 26 x 12 μm^3. The crystallographic texture in the center of the specimen was found to be primary of the Goss-type, as can be seen in Fig. 2(b) where an ODF (orientation distribution function) section at $\varphi_2 = 45°$ (Bunge notation) is shown. The crystallographic texture analysis was performed using X-ray diffraction on a 4-circle diffractometer of type Seifert PTS with Co-Kα radiation. Incomplete pole figures were determined for the {200}-, {220}-, {311}- and {222}-planes and evaluated using the MATLAB-toolbox MTEX [41] (as described in [37]).

Residual Stress Analysis

RS analysis near the surface was done on a companion specimen (i.e., a specimen built using the same parameters and from the same region as the CT-specimen) using IHD. Here, IHD was used as it is the laboratory method of choice when a depth information of the RS profile is of interest. Furthermore, IHD also allows to consider the crystallographic texture [40]. The lattice strain distributions in the center of the specimen were determined non-destructively using high-energy synchrotron X-ray diffraction in transmission mode.

Incremental hole-drilling method

The local macroscopic RS depth profile near the surface was analyzed using IHD according to ASTM E837-20 [42]. For drilling, a TiN-coated end mill with a nominal diameter of Ø 1.6 mm and a milling guide type RS200 (Vishay Measurements Group GmbH, Heilbronn, Germany), equipped with an air turbine, were used. To record the strain relaxation after each drilling increment a strain gauge rosette of type CEA-06-062UM-120 (Vishay Measurements Group GmbH, Heilbronn, Germany), which is equivalent to type B according to the ASTM E837-20, was used. The strain gauge rosette was aligned specifically, i.e., the strain gauge at 0° is aligned with BD and the strain gauge at 90° with TD. After drilling of the last increment, the actual hole diameter was determined using an optical microscope. Damped cubic spline functions were used to condition the strain relaxation data for evaluation. The RS calculation was done using the differential approach [43]. In order to take the elastic anisotropy imposed by the local crystallographic texture into account (as reported in [37]), the evaluation approach proposed in [40] was applied. For this approach a case-sensitive

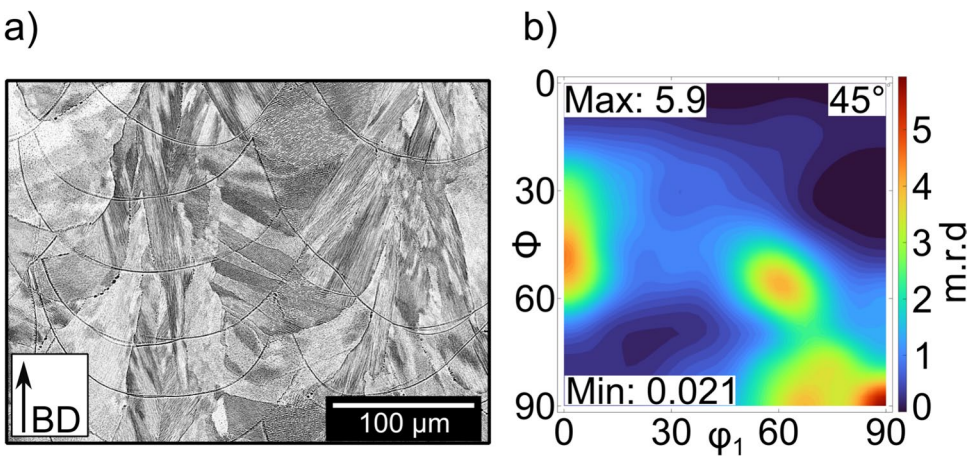

Fig. 2 (**a**) SEM-BSE image after etching with V2A-etchant (**b**) ODF-section at $\varphi_2 = 45°$ for the center of the specimen (2 mm depth) determined by XRD texture analysis

calibration is needed, which is based on the local ODF. The required ODF was determined by means of lab X-ray texture analysis (cf. Figure 2(b) – please note that data for the bulk material is shown in this case. Specimen handling is known to have an effect on the RS distribution, e.g. when CT-specimens from the walls of the tube profiles are extracted. In order to determine the RS depth profiles in a condition geometrically close to the CT-specimens, IHD was used on a cut open rectangular tube profile as depicted in Fig. 4 on the outside surface as well as on the inside surface of the tube profile.

Conical slit setup for high-energy synchrotron X-ray diffraction

In order to gain insights into the local strain distribution in the vicinity of the fatigue cracks, strain maps were determined at beamline P07 at PETRA III, DESY (operated by Helmholtz-Zentrum Hereon GmbH, Germany) on CT-specimens in two different conditions, i.e., with and without a grown crack, using high-energy synchrotron X-ray diffraction in transmission mode. In order to restrict the gauge volume to the center of the investigated specimens, a conical slit cell with individual conical slits for three {hkl}-planes was positioned in between the specimen and the detector as schematically shown in Fig. 3(a) and (b). The photon energy must be adjusted to the design of the conical slit cell, whose slits each have a gap size of 20 µm. Here, a photon energy of 67.63 keV, with a corresponding wavelength of 0.1833 Å was set by means of the monochromator, to allow for the analysis of the Debye–Scherrer rings of the {111}-, {200}- and {311}- crystallographic planes. The diffraction signal was recorded using a Perkin Elmer 2D-detector of type XRD 1621 xN ES, with 2048 × 2048 pixels and a pixel pitch of 200 µm. An example of the obtained diffraction signal is shown in Fig. 3(c).

Using this conical slit setup the length of the gauge volume along the beam direction can be adjusted. The focal distance, i.e., the distance between the specimen and the conical slit cell was set to nominally 100 mm. The length of the gauge volume was adjusted by changing the beam size (once the beam energy is fixed), to limit the gauge volume length along the beam direction to 1.23 mm, determined by the full width at half maximum (2.3 mm tail to tail). The length of the gauge volume was determined during the alignment by a scan along the beam path. Subsequently, the setup was adjusted to place the gauge volume into the center of the 4 mm thick CT-specimens. The beam size was set to $200 \times 200\ \mu m^2$. However, the chosen primary beam size was a compromise between a high spatial resolution (that was aimed for) and the grain size of the PBF-LB/M build material that would benefit from a larger beam size.

The mapping areas were varied between the specimens with and without a grown crack. In the specimen without a grown crack, the step size between measurement points was 0.32 mm along the x- and the y-axis, respectively. In the specimen with a grown crack, two overlapping and offset mappings (both with a step size of 0.4 mm in x- and y-direction, respectively) were used in order to increase the number of measurement points in the area in immediate vicinity of the crack. The offset between the two mappings is 0.2 mm along the x- and y-axis leading to a step size of 0.2 mm in x- and y-direction within the overlapping area around the crack.

Data Evaluation The determination of the detector center as well as the detector tilt correction was performed using the software tool pyFAI [44] based on a measurement carried out for LaB_6 powder using the same measuring conditions. For analysis of the measurement data, first a binning step for each measurement point was done by averaging the gray value of each pixel of the detector images over the nearest neighboring measurement points. In a subsequent step, an azimuthal integration using pyFAI with overlapping

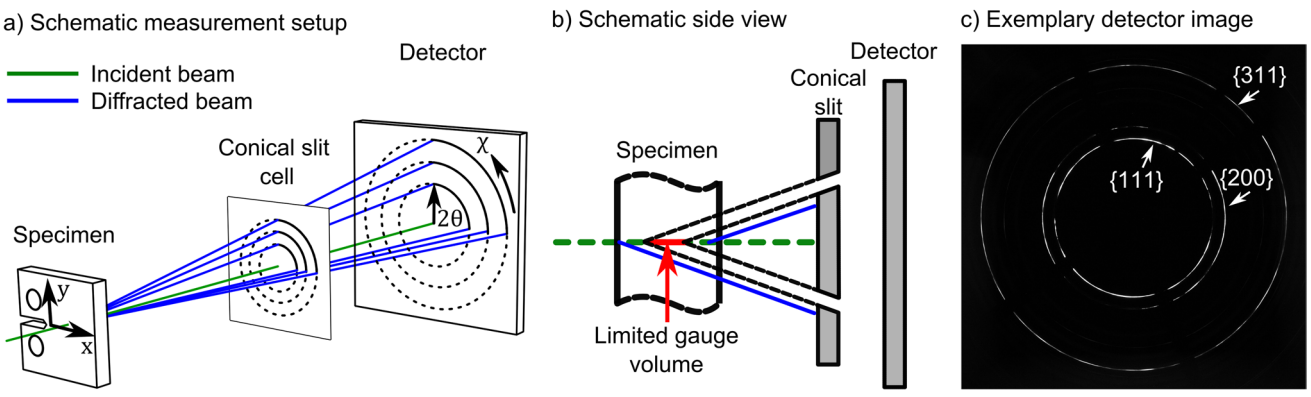

Fig. 3 Schematic of the conical slits setup, (**a**) position of the conical slit cell and indication of sample coordinate system (x,y), (**b**) side view showing the limited gauge volume (**c**) example diffraction result

cakes was performed. Here, a cake size of 10° was chosen with the cake centers being separated by 5°, leading to an overlap of 5° between adjacent cakes. Binning of measurement points and the cake size were considered to reduce the effect of the rather large grain size compared to the actual gauge volume defined by the primary beam size and the openings of the conical slits. The 2θ positions were determined using a Pseudo-Voigt function after background subtraction. The data from opposing cakes was averaged since they correspond to the same strain component in the specimen system. The determined 2θ positions were plotted over $\sin^2(\chi)$ as shown in Fig. 8(a), with χ being the azimuth angle (cf. Figure 3(a)). The 2θ vs. $\sin^2(\chi)$ distribution was then approximated linearly (cf. blue dotted line in Fig. 8(a)). Based on the values of the resulting linear function at the values $\sin^2(\chi)=0$ and $\sin^2(\chi)=1$ (highlighted in Fig. 8(a)), the lattice strains along 0° and 90°, which correspond to BD and TD, respectively, were calculated using equation (1). The necessary $2\theta_0$ value was determined based on a powder measurement of the AISI 316L powder used for PBF-LB/M manufacturing. The difference in the thermal history between the powder and the PBF-LB/M built CT-specimens might lead to a shift in 2θ, which has to be considered in the interpretation of the obtained diffraction results. Exemplary, the powder measurements were compared with individual small cubes with edge length of slightly below 2 mm sectioned from the PBF-LB/M built specimens. The maximum difference in 2θ corresponds to lattice strain of about 175 µm/m. Since it is not certain that the residual stresses in the cubes are sufficiently released by the sectioning process for the relatively inhomogeneous microstructure being present, the powder is used as $2\theta_0$ reference due to the rather small deviation in 2θ. Additionally, spatial variations of $2\theta_0$ can occur due to the additive manufacturing process, which are not taken into account. However, the CT-specimens are extracted from the mid-part of the rectangular tube profile and are therefore located at greater distance to regions where larger differences in e.g. the thermal history during the building process (corners or first-/last layer) are to be expected. In this report, only the results of the {311}-lattice planes are shown to demonstrate the general suitability of the measuring and evaluation approach, since these lattice planes most closely represent the macroscopic state of fcc (face-centered cubic) materials and are also considered insensitive to intergranular strains in the case of anisotropy [45]. Ultimately, the procedure followed allows to obtain an approximated linear distribution of 2θ vs. $\sin^2(\chi)$. To determine the uncertainties of the evaluated strain distributions, the 2θ uncertainties from the fitting process were propagated through the linear 2θ vs. $\sin^2(\chi)$ fit and the strain calculation using a Monte Carlo approach. Additionally, the standard deviation of the residuals from the linear fit was used to estimate the uncertainty resulting from non-ideal linear behavior. These two contributions were then combined in quadrature to obtain the stated strain uncertainties.

$$\varepsilon = -\frac{1}{2} cot\theta_0 * \left(2\theta - 2\theta_0\right) \tag{1}$$

Based on the $\sin^2(\psi)$ method [46], the stress difference ($\sigma_{90°}$-$\sigma_{0°}$) can be calculated from the linear fit function (of the 2θ vs. $\sin^2(\chi)$ distribution) using equation (2) with the X-ray diffraction elastic constant $\frac{1}{2}s_2^{\{311\}}$ and m being the slope of the linear 2θ vs. $\sin^2(\chi)$ approximation. Here, $\frac{1}{2}s_2^{\{311\}} = 7.11 * 10^{-6}\frac{1}{MPa}$ was applied, calculated using the model of Kröner and the single-crystal elastic constants from [47].

$$\left(\sigma_{90°} - \sigma_{0°}\right) = -\frac{1}{2} cot\theta_0 \frac{m}{\frac{1}{2}s_2} \tag{2}$$

X-ray Computed Tomography

To correlate the strain mapping results with the crack path, the actual crack path must be determined, as the potential drop method used to determine the crack length during fatigue loading cannot represent the actual crack path (in terms of lateral appearance). To monitor the actual crack path, micron computed tomography scans, using a micron computed tomograph (µCT) from Yxlon (Comet Yxlon GmbH, Hamburg, Germany), were carried out. 2100 projections were recorded using a direct emitter at a voltage of 200 kV and a current of 0.12 mA, providing a voxel size of around 9 μm^3. Reconstruction of the volume as well as the determination of the crack path, based on the change in the gray values, was performed using the software VGSTUDIO MAX (Volume Graphics GmbH/Hexagon, Heidelberg, Germany).

Results

Residual Stress Distribution Near Surface

In Fig. 4, the RS depth profiles near the surface on the outside as well as the inside of the cut open tube profile determined by IHD are shown. In Fig. 4(a) the specimen geometry is depicted with the red dot highlighting the measurement position on the outside surface. Along BD higher tensile RS are determined near the surface both on the outside and the inside of the prior tube profile as can be seen from the RS depth profiles in Fig. 4(b). In both cases, the depth range shown here indicates that there is a gradient of the RS distribution with increasing depth. On the outside, the tensile RS along BD decreases from around 250 MPa at a depth of approximately 0.15 mm,

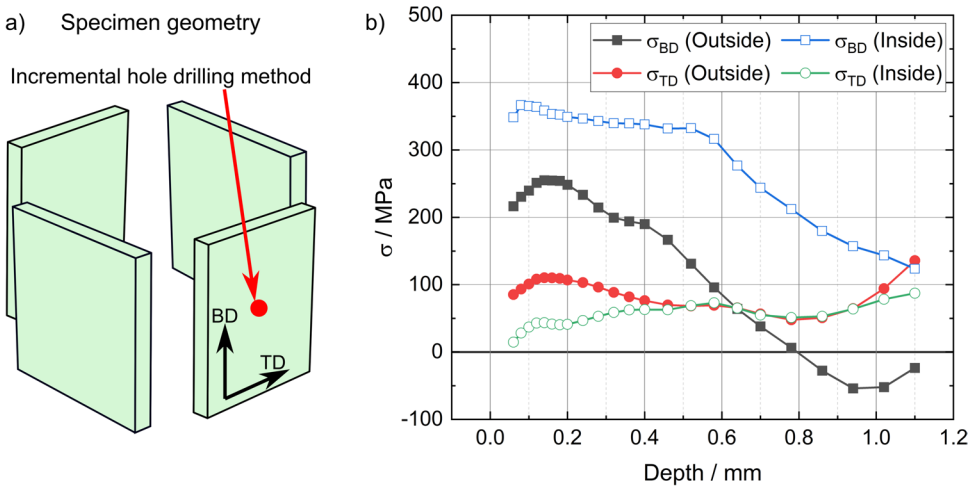

Fig. 4 (**a**) Specimen geometry (**b**) RS depth profiles near the surface determined using IHD

changing to compressive RS below a depth of around 0.8 mm (to about –50 MPa). On the inside, the tensile RS along BD are higher compared to the outside, being rather constant up to a depth of about 0.5 mm (at around 350 MPa), decreasing subsequently to about 120 MPa at a depth of approximately 1.1 mm.

Along TD, the RS are lower than along BD, both on the outside and on the inside of the tube profile. Furthermore, no pronounced in-depth gradient can be seen. Instead, the RS remain relatively constant, between about 50 to 100 MPa in both cases, with the RS on the inside near the surface being slightly lower than on the outside. It is important to note that the directions BD and TD are aligned with the principal stress directions.

Lattice Strain Mapping in the Center of the CT-specimen

In Fig. 5, the determined lattice strain distributions based on the diffraction result for the {311}-lattice planes in a CT-specimen in as-built condition, i.e., not subjected to fatigue loading and without a grown crack, respectively, are shown. Figure 5(a) additionally shows the coordinate system as well as the mapping area. The notch is introduced along TD by wire-EDM. During analysis, measurement points where the diffraction result is incomplete due to geometric features, such as the notch or the loading holes, are excluded from the analysis. Consequently, the shape of these features, shown in i.e. Figure 5(b) and (c), depends on the relative position of individual measurement points to these features. In Fig. 5(b), the determined lattice strain distribution along

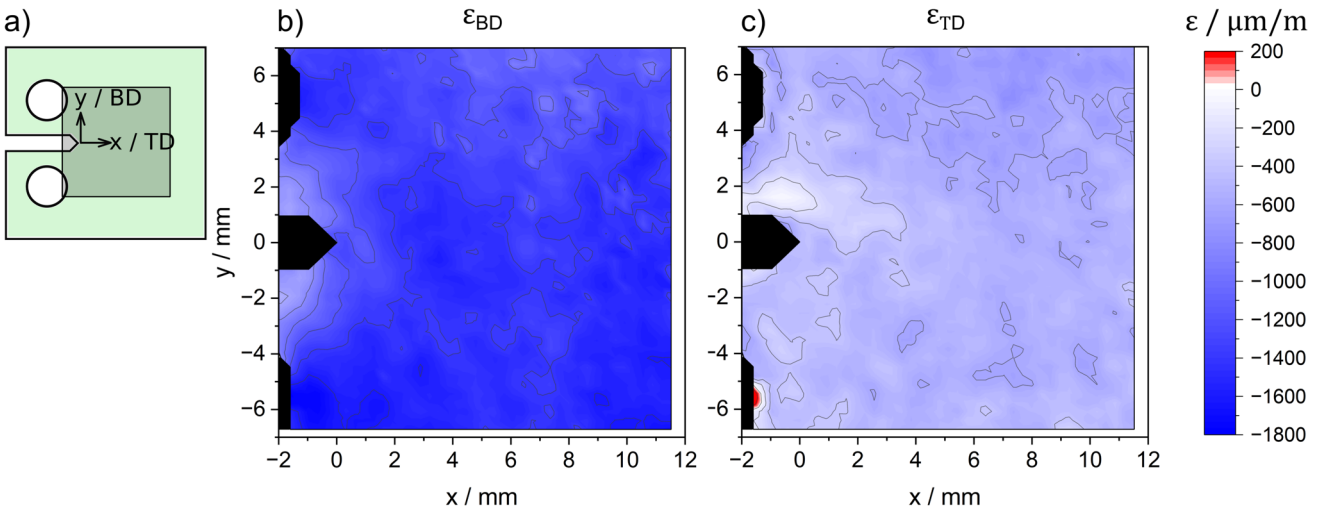

Fig. 5 Result of lattice strain mapping on a CT-specimen without grown crack, evaluated for the {311}-lattice planes: (**a**) Specimen-coordinate system and mapping region, (**b**) determined strain along BD, (**c**) determinded strain along TD

BD is shown. At larger distance from the machined features, a rather homogeneous compressive lattice strain distribution of around – 1700 to – 1400 µm/m can be seen. A small gradient along the y-axis/BD can be distinguished with the compressive lattice strain decreasing along BD. Next to the notch, a stronger decrease to about – 550 µm/m can be seen. Along TD (cf. Figure 5(c), the lattice strain distribution is rather homogeneous as well. However, the lattice strain is lower than in BD, being mostly around – 500 µm/m. Again, a gradient along y/BD can be seen with the compressive lattice strain increasing to around – 700 µm/m. Furthermore, near the notch a decrease in the lattice strain prevails. Due to the uncertainties in the determined 2θ values and the linear fit, the uncertainty in the determined strain values is around ± 135 µm/m for most measurement points in this sample.

In Fig. 6, the determined lattice strain distributions in the vicinity of a fatigue crack (growing parallel to BD) are shown. Figure 6(a) depicts the coordinate system as well as a rendering of the crack path as determined by X-ray computed tomography. Please note that (in direct comparison to the specimen before) the directions of BD and TD are rotated by 90° with BD being aligned with the x-axis. The crack grows rather straight and is not tilted across the wall thickness of the specimen. The crack length is around 6 mm (distance to the tip of the notch). The lattice strain distribution along BD, shown in Fig. 6(b) is rather homogeneous again in the area at a given distance from the crack, and in the compressive region between – 1800 and – 1500 µm/m. Near and in front of the crack as well as around the notch the lattice strain is lower, and even an almost strain free zone around the crack is observed, being characterized by lattice strain values of around – 120 µm/m. The area being characterized by a reduced lattice strain extends to around 2 mm in front of the crack tip, the latter feature being determined on basis of the X-ray computed tomography data. In addition, in this specimen a lower and rather homogeneous lattice strain distribution at a given distance to notch and crack, respectively, is determined along TD, with the compressive lattice strain being around – 400 to – 300 µm/m. In the crack wake the lattice strain is of higher magnitude being around – 900 to – 700 µm/m. In front of the crack tip an area being characterized by tensile lattice strain values of around 100 to 200 µm/m can be observed, eventually pinpointing local tensile strain. This area of tensile lattice strain has an extension of about 1 × 4 mm with the 4 mm edge oriented in direction of the y-axis. This zone with tensile lattice strains is surrounded by an area that is almost strain-free. Similarly, around the notch tip a decrease in lattice strain to an almost strain free state is determined. Due to the uncertainties in the determined 2θ values and the linear fit, the uncertainty in the determined strain values is around ± 120 µm/m for most measurement points in this sample.

In Fig. 7, the result of the lattice strain mapping for a CT-specimen with a crack growing perpendicular to BD is shown. In Fig. 7(a), the coordinate system and the two overlapping mapping areas are shown. Furthermore, a rendering of the crack path determined based on an X-ray computed tomography scan is shown. It can be seen that the crack does not grow perfectly perpendicular to BD, but is deflected downwards with a deflection angle of approximately 20° with the crack tip being around 2.5 mm lower

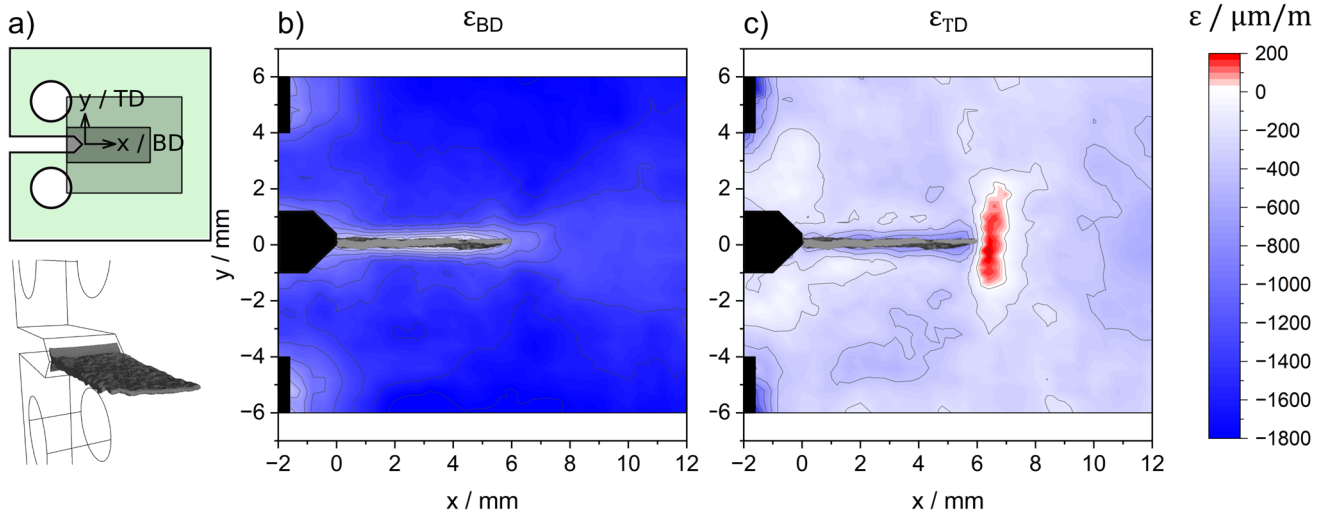

Fig. 6 Result of lattice strain mapping on a CT-specimen with crack growing parallel to BD, evaluated for {311}- lattice planes: (**a**) Specimen-coordinate system with mapping region and rendering of the crack path, (**b**) determined lattice strain along BD with superimposed crack path, (**c**) determinded lattice strain along TD with superimposed crack path. Please note that (in direct comparison to the specimens depicted in Fig. 5 and 7) the direction of BD and TD is rotated by 90°

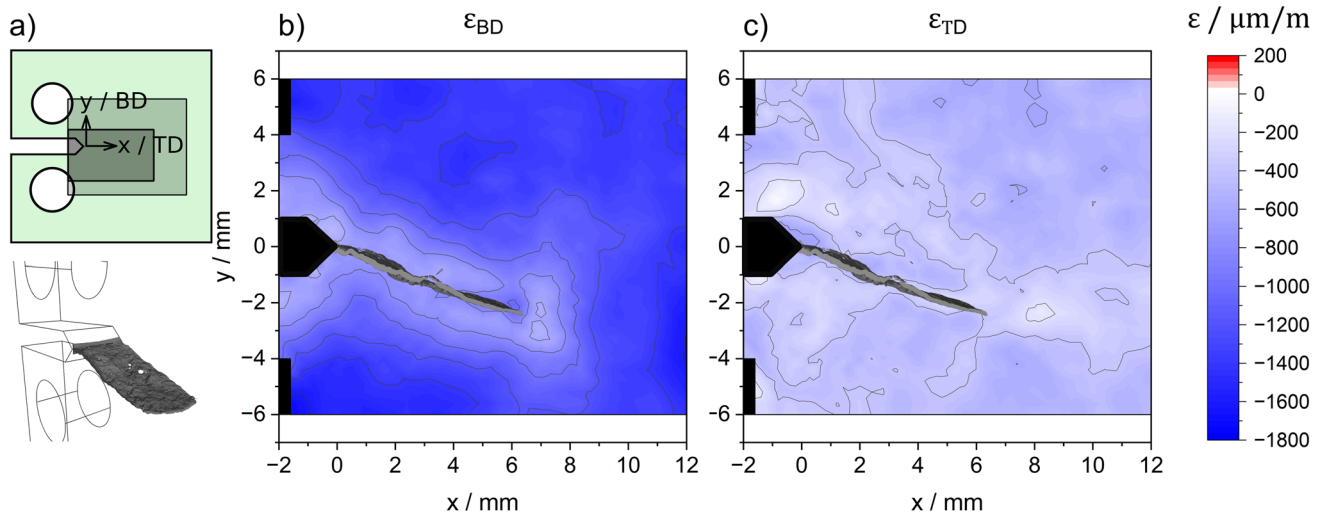

Fig. 7 Result of lattice strain mapping on a CT-specimen with crack growing perpendicular to BD, evaluated for {311}-lattice planes: (**a**) Specimen-coordinate system with mapping region and rendering of the crack path, (**b**) determined lattice strain along BD with superimposed crack path, (**c**) determinded lattice strain along TD with superimposed crack path

than the initiating horizontal plane of the crack. The crack tip is located around 6.5 mm from the tip of the notch. Across the wall thickness the crack grows rather planar only showing small deviations from that planar characteristic. In Fig. 7(b), the lattice strain distribution along BD based on the diffraction results of the {311}-lattice planes is shown. At larger distances to the notch and the grown crack, a rather homogeneous (compressive) lattice strain distribution can be seen. Similarly to the specimen without a grown crack, the compressive lattice strain is in the range of − 1500 to − 1300 µm/m. In the vicinity of the crack a decrease in the compressive lattice strain distribution is determined with the lattice strain being around − 700 to − 500 µm/m near the crack, except in the area right next to the crack tip, where the compressive lattice strain is of higher magnitude being around –1000 µm/m. Compared to the specimen with the crack growing parallel to BD, the area where a change in the lattice strain distribution around the crack is noticed is much wider (alongside the crack wake). Along TD the determined lattice strain is around − 500 µm/m, therefore lower than along BD. Above and below the crack, regions are seen with even lower lattice strain (about − 300 µm/m). However, the crack path is not that clearly distinguishable by the lattice strain values as in case of BD. Overall the lattice strain distribution is rather homogeneous. Due to the uncertainties in the determined 2θ values and the linear fit, the uncertainty in the determined strain values is around ± 110 µm/m for most measurement points in this sample.

In Fig. 8(a), the 2θ vs. $\sin^2(\chi)$ distribution for one measurement point is shown as an example. It can be seen that (beside some minor alterations) it generally follows an almost linear trend and therefore can be well approximated linearly without introducing a large error. In Fig. 8(b), the calculated stress difference (σ_{BD} - σ_{TD} which corresponds to $\sigma_{90°}$ - $\sigma_{0°}$ in equation (2) for the CT-specimen without a grown crack is shown as a result of the $\sin^2(\chi)$ evaluation of the 2D diffraction data. Since no information about the strain in the third direction is available, an evaluation of the stress distribution in one direction cannot be made without strict assumptions like a plane stress or plane strain state, which may also be erroneous. Therefore, only the stress difference was calculated and is shown here. The stress difference is rather homogeneous and compressive ranging from around − 150 to around − 75 MPa with a small gradient along the y-axis/BD. In Fig. 8(c), the calculated stress difference (σ_{BD} - σ_{TD}) for the CT-specimen with the crack growing parallel to BD is shown. In the crack wake, a positive (tensile stress) difference is seen, while above and below the crack the stress difference is compressive with a maximum of around − 250 to − 200 MPa. In front of the crack tip, a rather large area with a lower compressive stress difference of around − 150 to − 100 MPa is determined. In Fig. 8(d), the calculated stress difference (σ_{BD} - σ_{TD}) for the CT-specimen with the crack growing perpendicular to BD is shown. At larger distances to the notch and the grown crack, the stress difference is compressive at around − 120 MPa while in the vicinity of the crack the stress difference is reduced to around − 50 MPa.

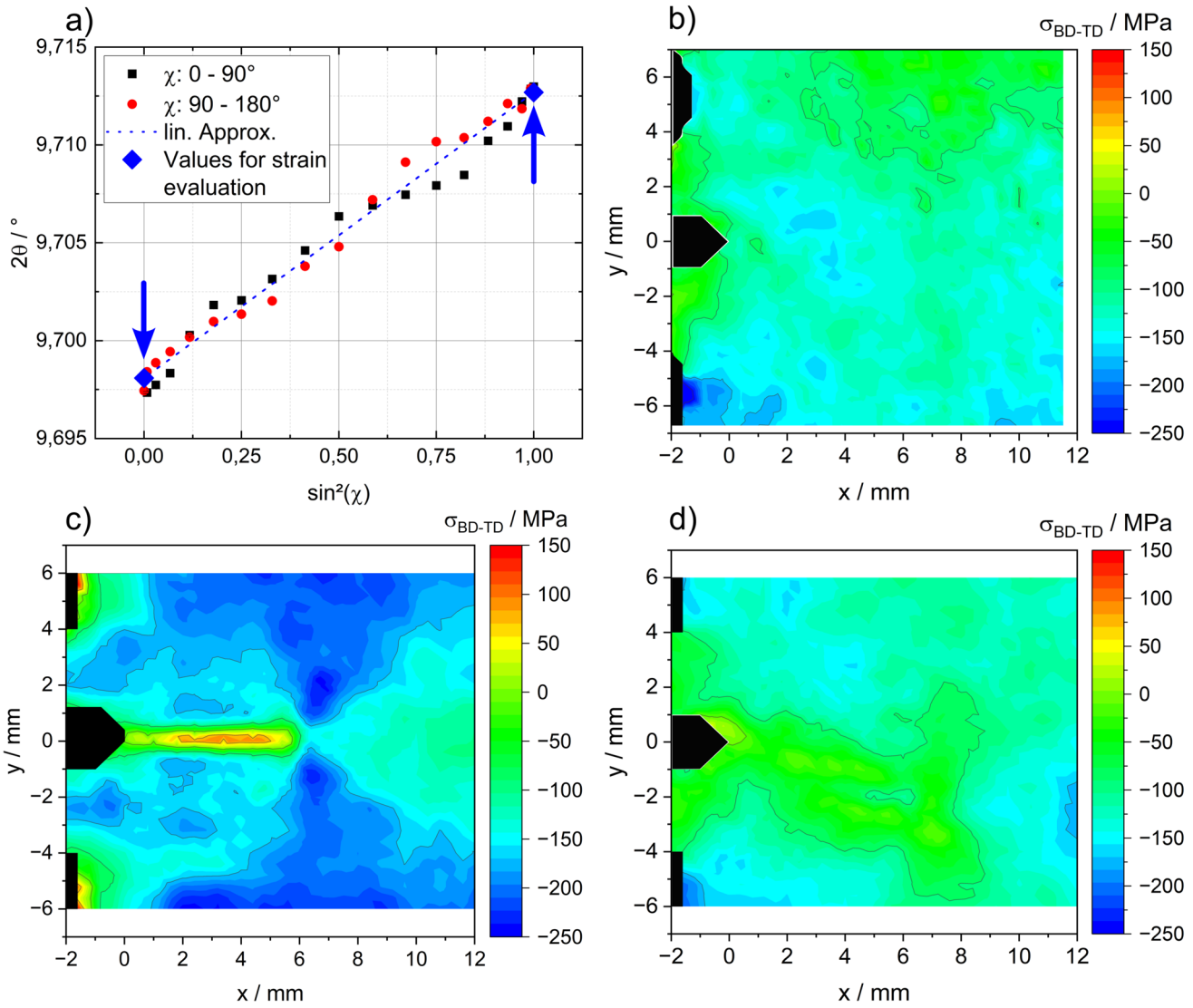

Fig. 8 (**a**) Exemplary 2θ vs. $\sin^2(\chi)$ distribution; (**b**) calculated stress-difference (σ_{BD} - σ_{TD}) for the CT-specimen without grown crack; (**c**) calculated stress-difference (σ_{BD} - σ_{TD}) for the CT-specimen with the crack growing parallel to BD (**d**) calculated stress-difference (σ_{BD} - σ_{TD}) for the CT-specimen with the crack growing perpendicular to BD

Discussion

Residual Stress Distribution Near the Surface

The RS depth profiles near the surface determined by means of IHD (cf. Figure 4) show higher tensile RS near the surface along BD with an in-depth gradient towards the center of the specimen, while the RS along TD remains on a relatively constant level of lower magnitude. This type of RS distribution is also characteristic for the as-built state as reported in [37], although at higher magnitudes, especially along BD. Similarly, [48] also found higher tensile RS near the surface as well as compressive RS in the center of the structure as a result of RS equilibrium, characterized by using neutron diffraction and DIC in thin L-shaped brackets made out of PBF-LB/M processed 316L. The larger temperature gradient at the surface leads to a higher level of RS. The difference between the outside surface and the inside surface is most likely caused by the difference in geometric constraints by the original tube profile shape and the removal of this geometric constraint through sectioning. The opening of the tube profile was done from the outside towards the inside surface. Therefore, during cutting the geometric constraints were already removed on and near the outside surface, enabling an elastic redistribution of the RS, while the region near the inside surface was still constrained.

The in-depth gradient in the RS along BD makes it necessary to restrict the gauge volume to the center of the

specimens by the conical slits. This enables the evaluation of the influence of the RS distribution in the bulk of the specimen, which, in our opinion, appears more relevant for assessing the crack propagation behavior, separate from the RS near the surface. In a conventional transmission setup, the diffraction result would be integrated over the full specimen thickness, including the in-depth gradient determined at the surface by means of IHD. Based on the RS distribution near the surface, compressive RS in the center of the specimen are expected to balance the tensile RS near the surface, with these balancing compressive RS being of higher magnitude along BD than along TD.

Lattice Strain Mapping in Center of Specimen

The use of conical slits leads to a decrease in diffracted intensity in comparison to a conventional transmission experiment without conical slits. Paired with the rather small beam size of 200×200 µm^2 (compared to a grain size of around $73 \times 26 \times 12$ µm^3 [37]), the statistics of the diffraction data received were rather limited. This makes it necessary to use a rather large cake size of 10° for evaluating the 2D diffraction data as well as the binning of measurement points. The averaging of opposing cakes increases the statistics further and is common practice for the application of conical slits and for a transmission measurement, since for the high beam energy and resulting small 2θ-angles (< 10°) the difference in the scattering vector is rather small, hence this has a minor effect on strain and stress calculation and can be neglected. To evaluate the lattice strain along BD and TD, respectively, either the 2θ-position from the corresponding cakes can be used or as described before, the values of a linear fit over $\sin^2(\chi)$ at $\sin^2(\chi) = 0$ and $\sin^2(\chi) = 1$, depending on the definition of the azimuthal angle with respect to the coordinate system. The evaluation using the linear fit assumes that a potential influence of a crystallographic texture as well as the influence of intergranular strains is rather negligible. If this is the case, this approach provides a statistically solid result of the determined lattice strain, as not only single cakes but the information from the complete Debye–Scherrer ring is considered. In case of the analyzed CT-specimens, a crystallographic texture is present as reported in [37] and shown in Fig. 2(b). The exemplary 2θ vs. $\sin^2(\chi)$ plot in Fig. 8(a) indicates that no strong nonlinear (oscillating) 2θ vs. $\sin^2(\chi)$ distributions are observed and, therefore, the influence of the crystallographic texture and the intergranular strains is rather negligible.

In the areas at larger distance from features like the notch or the crack, all lattice strain distributions within the different CT-specimens show a compressive lattice strain for the {311}-lattice planes (cf. Figure 5, 6, and 7). Based on the tensile RS near the surface, determined by IHD, balancing compressive RS in the center of the specimen are assumed. Due to the limitation of the gauge volume to the center of the specimen by the conical slits, the determined compressive lattice strain confirms the presence of balancing compressive RS. This is also the case with respect to the magnitude, with both tensile RS near the surface and compressive lattice strain in the center of the specimen being of higher magnitude along BD compared to along TD. However, a direct quantitative comparison between results obtained via IHD and those derived from lattice strain mappings determined by diffraction methods might be misleading, as the underlying measurement principles differ fundamentally (macroscopic stresses vs. elastic lattice strain) and the measurement volumes vary significantly. The magnitude of the compressive lattice strain along BD and TD is literally consistent over the three different specimens, indicating a reproduceable RS state by the manufacturing process. Additionally, the compressive lattice strain is rather homogeneous over BD. The absence of a distinct gradient over BD is in line with the determined RS profiles reported in [37], where also no strong or distinct gradient over the side of the tube profile along BD was reported. Around the notch, the lattice strain along BD and TD is reduced. This change in the residual strain distribution is most likely caused by manufacturing the CT-specimen geometry using wire-EDM, causing a partial strain relaxation but also introducing characteristic EDM-machining residual strain distributions.

Along BD, in the area that exhibits a higher and rather homogeneous compressive lattice strain, the growing crack leads to a strain relaxation along its path. Independent of the crack growth direction (parallel or perpendicular to BD), the lattice strain distribution in the vicinity of the crack is significantly reduced (cf. Figure 6(b) and Fig. 7(b)). In case of the crack growing parallel to BD, the crack grows in a rather horizontal path, whereas in case of the crack growing perpendicular to BD it gets deflected. The reason for the deflection of the crack is still not fully understood yet, but can be reproduced and is likely caused by a microstructure effect induced by PBF-LB/M. With the crack growing parallel to BD without deflection (cf. Figure 6(b)), the strain relaxation is on the one hand much more localized around the crack path, and on the other hand more pronounced, eventually resulting in an almost lattice strain free state in the direct vicinity of the crack. The crack growing perpendicular to BD, which gets deflected (cf. Figure 7(b)), leads to strain relaxation in a larger area, however, no strain-free state is found, rather only a reduced lattice strain in the vicinity of the crack. The reason for the larger affected area is also not yet fully understood, since both cracks, as can be seen in the respective computed-tomography scan, grow rather planar over the wall-thickness of the CT-specimen. Therefore, this might be caused by the prevailing grain morphology. Here, current work is ongoing and will be addressed in a follow-up paper.

Along the crack opening direction, as stated in [49], during cyclic loading a monotonic plastic zone in front of the crack tip develops, with a reverse plastic zone (smaller in size) occurring during the unloading step inside this plastic zone right at the crack tip. This results in a compressive stress distribution at the crack tip within the region of the reverse plastic zone and a tensile stress region in the remaining monotonic plastic zone, the latter being located in larger distance to the crack tip [50]. Such a distribution was also determined by the authors in [28] and [31] experimentally using EDXRD, where they found a compressive strain field surrounding the crack path and a tensile strain region in front of the crack tip along the crack opening direction.

In the CT-specimen, with the crack growing parallel to BD (cf. Figure 6(c)), the crack opening direction is along TD, with an initial compressive lattice strain state of lower magnitude. In front of the crack tip, a region of minor tensile lattice strain is observed. Since no load is applied during the mapping experiment combined with the initial compressive lattice strain state, the magnitude of the tensile lattice strain region in front of the crack tip was anticipated to be rather low. Along the crack, the lattice strain is compressive at a higher magnitude compared to both the region at a larger distance from the crack and the crack-free specimen condition, again being in good agreement with findings in literature. Both regions (tensile in front of the crack tip, compressive around the crack) are easily distinguishable due to the lower magnitude of the compressive lattice strain state (cf. Figure 6(b).

In contrast, in the CT-specimen with the crack growing perpendicular to BD (cf. Figure 7(b)), the crack opening direction is along BD, with the higher magnitude compressive residual lattice strain in the initial state. As already discussed, the crack leads to a strain relaxation along its path (cf. Figure 6(b), Fig. 7(b)). The compressive strain developing around the crack path and especially right at the crack tip along the crack opening direction, however counteracts this strain relaxation. This might explain the previously mentioned lower amount of lattice strain relaxation along BD in this CT-specimen. Particularly right at the crack tip, where the compressive strain along the crack opening direction should be the highest based on the reverse plastic zone, the determined compressive lattice strain is also the highest in the vicinity of the crack. In front of the crack tip, an area of lower compressive lattice strain is visible, corresponding to the region where a tensile strain region might develop along the crack opening direction. However, due to the higher magnitude of compressive lattice strain along BD, only a more substantial decrease in the compressive lattice strain can be determined, being in good agreement with literature.

With the current experimental setup, no tilting or rotation of the specimen has been conducted, which makes the third strain component along the beam direction inaccessible. An evaluation of the stress distribution in one direction, based on the determined lattice strain distributions, can therefore only be made by assuming either a plane stress or a plane strain state, i.e., by making tough assumptions which cannot be confirmed at the current state. Without either of these two assumptions, only a stress difference, as shown in Fig. 8(b–d), can be calculated. This already enables the interpretation of the stress distribution when combined with the additional knowledge of the lattice strain along both directions. These determined distributions (stress difference and lattice strain) enable future assessments of the effects of the RS distributions on the crack growth behavior by using the distributions as input data for fracture mechanics simulations.

Conclusions

In the present study, the lattice strain distributions in the vicinity of fatigue cracks in the mid-plane of CT-specimens made of PBF-LB/M manufactured AISI 316L were determined using a combined approach including IHD and mapping experiments exploiting monochromatic high-energy synchrotron X-ray radiation coupled with a conical slit setup. From the experimental findings, the following conclusions can be drawn:

- The proposed strategy to determine the strain distributions is appropriate to map the lattice strain in the vicinity of cracks in the center of specimens with a high lateral resolution.
- The used conical slits for the {111}-, {200}- and {311}-crystallographic planes restrict the gauge volume to the area around the specimens' middle plane, enabling the separation of the bulk strain distribution from the near surface areas.
- The usage of a complementary laboratory RS analysis method (IHD) enables a holistic assessment of the RS distributions and supports the interpretation of the determined lattice strain mappings, enabling the future assessment of related effects on the crack propagation through, e.g., simulations using the determined lattice strain distributions as input data.
- The PBF-LB/M process leads to tensile RS near the surface that get balanced by compressive RS in the bulk of the specimen, with a higher magnitude along BD than TD.
- Compressive lattice strain gets significantly reduced in the vicinity of the cracks. Depending on the residual lattice strain magnitude, a tensile lattice strain region might develop in front of the crack tip without any applied load.

- In case of the crack growing perpendicular to BD, the crack gets significantly deflected, which is likely caused by a microstructure effect induced by PBF-LB/M.

Acknowledgements The authors gratefully acknowledge funding by German Research Foundation (DFG), grant no. 505457585. We also acknowledge DESY (Hamburg, Germany), a member of the Helmholtz Association HGF, for the provision of experimental facilities. Parts of this research were carried out at PETRA III. Data was collected using beamline P07 (EH3) operated/provided by Helmholtz-Zentrum Hereon. Beamtime was allocated for proposal I-20230499."

Author Contributions Florian Loebich: conceptualization, data curation, formal analysis, investigation, methodology, validation, visualization, writing-original draft, writing-review and editing. Nico Möller: conceptualization, resources, investigation, writing-review and editing. Julia Richter: conceptualization, investigation, writing-review and editing. Thomas Wegener: conceptualization, writing-review and editing. David Canelo-Yubero: resources, writing-review and editing. Emad Maawad: resources, writing-review and editing. Norbert Schell: resources, writing-review and editing. Jens Gibmeier: conceptualization, methodology, funding acquisition, supervision, project administration, writing-review and editing. Thomas Niendorf: methodology, funding acquisition, supervision, project administration, writing-review and editing.

Funding Open Access funding enabled and organized by Projekt DEAL. This project was funded by the German Research Foundation (DFG) through the project 505457585.

Data Availability The data underlying the results presented in this paper are not publicly available at this time but may be obtained from the authors upon reasonable request.

Declarations

Competing interests The authors declare that they have no known competing financial interests or personal relationships that could have appeared to influence the work reported in this paper.

Open Access This article is licensed under a Creative Commons Attribution 4.0 International License, which permits use, sharing, adaptation, distribution and reproduction in any medium or format, as long as you give appropriate credit to the original author(s) and the source, provide a link to the Creative Commons licence, and indicate if changes were made. The images or other third party material in this article are included in the article's Creative Commons licence, unless indicated otherwise in a credit line to the material. If material is not included in the article's Creative Commons licence and your intended use is not permitted by statutory regulation or exceeds the permitted use, you will need to obtain permission directly from the copyright holder. To view a copy of this licence, visit http://creativecommons.org/licenses/by/4.0/.

References

1. Herzog D, Seyda V, Wycisk E, Emmelmann C (2016) Additive manufacturing of metals. Acta Mater 117:371–392. https://doi.org/10.1016/j.actamat.2016.07.019
2. DebRoy T, Wei HL, Zuback JS et al (2018) Additive manufacturing of metallic components – Process, structure and properties. Prog Mater Sci 92:112–224. https://doi.org/10.1016/j.pmatsci.2017.10.001
3. Chowdhury S, Yadaiah N, Prakash C et al (2022) Laser powder bed fusion: a state-of-the-art review of the technology, materials, properties & defects, and numerical modelling. J Mater Res Technol 20:2109–2172. https://doi.org/10.1016/j.jmrt.2022.07.121
4. Kruth JP, Badrossamay M, Yasa E et al (2010) Part and material properties in selective laser melting of metals. Proc. 16th Int. Symp. Electromachining (ISEM XVI) 3–14
5. Popovich VA, Borisov EV, Popovich AA et al (2017) Functionally graded Inconel 718 processed by additive manufacturing: Crystallographic texture, anisotropy of microstructure and mechanical properties. Mater Des 114:441–449. https://doi.org/10.1016/j.matdes.2016.10.075
6. Niendorf T, Leuders S, Riemer A et al (2014) Functionally graded alloys obtained by additive manufacturing. Adv Eng Mater 16:857–861. https://doi.org/10.1002/adem.201300579
7. Brenne F, Niendorf T (2019) Damage tolerant design by microstructural gradation – Influence of processing parameters and build orientation on crack growth within additively processed 316L. Mater Sci Eng A 764:138186. https://doi.org/10.1016/j.msea.2019.138186
8. Mercelis P, Kruth JP (2006) Residual stresses in selective laser sintering and selective laser melting. Rapid Prototyp J 12:254–265. https://doi.org/10.1108/13552540610707013
9. Kumar VP, Jebaraj AV (2023) Comprehensive review on residual stress control strategies in laser-based powder bed fusion process– Challenges and opportunities. Lasers Manuf Mater Process 10:400–442. https://doi.org/10.1007/s40516-023-00217-6
10. Wang L, Jiang X, Zhu Y et al (2018) An approach to predict the residual stress and distortion during the selective laser melting of AlSi10Mg parts. Int J Adv Manuf Technol 97:3535–3546. https://doi.org/10.1007/s00170-018-2207-3
11. Balbaa M, Elbestawi M (2022) Multi-scale modeling of residual stresses evolution in laser powder bed fusion of inconel 625. J Manuf Mater Process 6:2. https://doi.org/10.3390/jmmp6010002
12. Xia M, Gu D, Yu G et al (2016) Influence of hatch spacing on heat and mass transfer, thermodynamics and laser processability during additive manufacturing of Inconel 718 alloy. Int J Mach Tools Manuf 109:147–157. https://doi.org/10.1016/j.ijmachtools.2016.07.010
13. Dong Z, Liu Y, Wen W et al (2019) Effect of hatch spacing on melt pool and as-built quality during selective laser melting of stainless steel: modeling and experimental approaches. Materials (Basel) 12:50. https://doi.org/10.3390/ma12010050
14. Liu Y, Yang Y, Wang D (2016) A study on the residual stress during selective laser melting (SLM) of metallic powder. Int J Adv Manuf Technol 87:647–656. https://doi.org/10.1007/s00170-016-8466-y
15. Yadroitsev I, Yadroitsava I (2015) Evaluation of residual stress in stainless steel 316L and Ti6Al4V samples produced by selective laser melting. Virtual Phys Prototyp 10:67–76. https://doi.org/10.1080/17452759.2015.1026045
16. Jia H, Sun H, Wang H et al (2021) Scanning strategy in selective laser melting (SLM): a review. Int J Adv Manuf Technol 113:2413–2435. https://doi.org/10.1007/s00170-021-06810-3
17. Zhang W, Tong M, Harrison NM (2020) Scanning strategies effect on temperature, residual stress and deformation by multi-laser beam powder bed fusion manufacturing. Addit Manuf 36:101507. https://doi.org/10.1016/j.addma.2020.101507
18. McClung RC (2007) A literature survey on the stability and significance of residual stresses during fatigue. Fatigue Fract Eng Mater Struct 30:173–205. https://doi.org/10.1111/j.1460-2695.2007.01102.x

19. Leuders S, Thöne M, Riemer A et al (2013) On the mechanical behaviour of titanium alloy TiAl6V4 manufactured by selective laser melting: Fatigue resistance and crack growth performance. Int J Fatigue 48:300–307. https://doi.org/10.1016/j.ijfatigue.2012.11.011
20. James MN, Hughes DJ, Chen Z et al (2007) Residual stresses and fatigue performance. Eng Fail Anal 14:384–395. https://doi.org/10.1016/j.engfailanal.2006.02.011
21. Garcia C, Lotz T, Martinez M et al (2016) Fatigue crack growth in residual stress fields. Int J Fatigue 87:326–338. https://doi.org/10.1016/j.ijfatigue.2016.02.020
22. Vrancken B (2016) Study of residual stresses in selective laser melting. Dissertation, KU Leuven
23. Jiang W, Yu Y, Zhang W et al (2020) Residual stress and stress fields change around fatigue crack tip: neutron diffraction measurement and finite element modeling. Int J Press Vessel Pip 179:104024. https://doi.org/10.1016/j.ijpvp.2019.104024
24. Jägg S, Scholtes B (2005) Crack-tip residual stresses and crack propagation in cyclically-loaded specimens under different loading modes. Zeitschrift fuer Metallkd 96:770–774. https://doi.org/10.3139/146.101100
25. Steuwer A, Daniels JE (2011) In-situ stress and strain measurements around cracks using synchrotron X-ray diffraction. J Strain Anal Eng Des 46:593–606. https://doi.org/10.1177/0309324711408501
26. Lee SY, Sun Y, An K et al (2010) Evolution of residual-strain distribution through an overload-induced retardation period during fatigue-crack growth. J Appl Phys 107:023517. https://doi.org/10.1063/1.3234388
27. Lee SY, Choo H, Liaw PK et al (2011) A study on fatigue crack growth behavior subjected to a single tensile overload: Part II. Transfer of stress concentration and its role in overload-induced transient crack growth. Acta Mater 59:495–502. https://doi.org/10.1016/j.actamat.2010.09.048
28. Steuwer A, Santisteban JR, Turski M et al (2004) High-resolution strain mapping in bulk samples using full-profile analysis of energy-dispersive synchrotron X-ray diffraction data. J Appl Crystallogr 37:883–889. https://doi.org/10.1107/S0021889804023349
29. Croft M, Zhong Z, Jisrawi N et al (2005) Strain profiling of fatigue crack overload effects using energy dispersive X-ray diffraction. Int J Fatigue 27:1408–1419. https://doi.org/10.1016/j.ijfatigue.2005.06.022
30. Kerr M, Daymond MR, Holt RA, Almer JD (2010) Mapping of crack tip strains and twinned zone in a hexagonal close packed zirconium alloy. Acta Mater 58:1578–1588. https://doi.org/10.1016/j.actamat.2009.10.064
31. Steuwer A, Rahman M, Shterenlikht A et al (2010) The evolution of crack-tip stresses during a fatigue overload event. Acta Mater 58:4039–4052. https://doi.org/10.1016/j.actamat.2010.03.013
32. Poulsen HF, Garbe S, Lorentzen T et al (1997) Applications of high-energy synchrotron radiation for structural studies of polycrystalline materials. J Synchrotron Radiat 4:147–154. https://doi.org/10.1107/S0909049597002021
33. Staron P, Fischer T, Eims EH et al (2014) Depth-resolved residual stress analysis with conical slits for high-energy X-rays. Mater Sci Forum 772:3–7. https://doi.org/10.4028/www.scientific.net/MSF.772.3
34. Staron P, Fischer T, Keckes J et al (2014) Depth-resolved residual stress analysis with high-energy synchrotron X-rays using a conical slit cell. Mater Sci Forum 768:72–75. https://doi.org/10.4028/www.scientific.net/MSF.768-769.72
35. Hayashi Y, Setoyama D, Fukuda K et al (2023) Scanning three-dimensional X-ray diffraction microscopy with a spiral slit. Quantum Beam Sci 7:16. https://doi.org/10.3390/qubs7020016
36. Sinsheimer J, Bouet N, Ghose S et al (2016) Fabrication and testing of a newly designed slit system for depth-resolved X-ray diffraction measurements. J Synchrotron Radiat 23:1296–1304. https://doi.org/10.1107/S1600577516013084
37. Möller N, Loebich F, Wegener T et al (2025) Residual stress States in microstructurally graded PBF–LB/M austenitic steel components. Adv Eng Mater. https://doi.org/10.1002/adem.202500412
38. Olson MD, DeWald AT, Hill MR (2020) Precision of hole-drilling residual stress depth profile measurements and an updated uncertainty estimator. Exp Mech 61:549–564. https://doi.org/10.1007/s11340-020-00679-1
39. Lakey MC, Hill MR (2024) Validation of hole-drilling residual stress measurements in workpieces of various thickness. Exp Mech 64:1529–1544. https://doi.org/10.1007/s11340-024-01107-4
40. Schuster S, Gibmeier J (2016) Incremental hole drilling for residual stress analysis of strongly textured material states – a new calibration approach. Exp Mech 56:369–380. https://doi.org/10.1007/s11340-015-0104-3
41. Bachmann F, Hielscher R, Schaeben H (2010) Texture analysis with mtex- free and open source software toolbox. Solid State Phenom 160:63–68. https://doi.org/10.4028/www.scientific.net/SSP.160.63
42. ASTM E837–20 (2022) Standard test method for determining residual stresses by the hole-drilling strain-gage method. Stand. Test Method E837–20 i:1–16. https://doi.org/10.1520/E0837-20.1
43. Schwarz T, Kockelmann H (1993) Die Bohrlochmethode - ein für viele Anwendungsbreiche optimales Verfahren zur experimentellen Ermittlung von Eigenspannungen. Messtechnische Briefe 29:33–38
44. Kieffer J, Wright JP (2013) PyFAI: a Python library for high performance azimuthal integration on GPU. Powder Diffr 28:339–350. https://doi.org/10.1017/S0885715613000924
45. Clausen B, Leffers T, Lorentzen T (2003) On the proper selection of reflections for the measurement of bulk residual stresses by diffraction methods. Acta Mater 51:6181–6188. https://doi.org/10.1016/j.actamat.2003.07.002
46. Hauck V (1997) Structural and residual stress analysis by nondestructive methods. Elsevier, Amsterdam
47. Charmi A, Falkenberg R, Ávila L et al (2021) Mechanical anisotropy of additively manufactured stainless steel 316L: an experimental and numerical study. Mater Sci Eng A 799:140154. https://doi.org/10.1016/j.msea.2020.140154
48. Wu AS, Brown DW, Kumar M et al (2014) An experimental investigation into additive manufacturing-induced residual stresses in 316L stainless steel. Metall Mater Trans A 45:6260–6270. https://doi.org/10.1007/s11661-014-2549-x
49. Rice JR (1968) Mathematical analysis in the mechanics of fracture. In: Liebowitz H (ed) Fracture: an advanced treatise. Academic Press, New York, pp 191–311
50. Jingjie C, Yi H, Leilei D, Yugang L (2014) A new method for cyclic crack-tip plastic zone size determination under cyclic tensile load. Eng Fract Mech 126:141–154. https://doi.org/10.1016/j.engfracmech.2014.05.001

Publisher's Note Springer Nature remains neutral with regard to jurisdictional claims in published maps and institutional affiliations.